Creep Behavior of the Heusler Type Structure Alloy Ni_2AlTi

P. R. STRUTT, R. S. POLVANI, AND J. C. INGRAM

A specific method for improving the high temperature creep strength of β-NiAl by a ternary addition giving rise to an additional degree of order is examined. The ternary alloy thus formed has the A_2BC or Heusler type structure, and the present study is devoted to the creep behavior of polycrystalline Ni_2AlTi of stoichiometric composition. Possible slip modes are predicted on the basis of the hard sphere model, and quantitative transmission electron microscopy is used to verify these predictions. All intracellular dislocations, and network dislocations have a $a_0\langle 110\rangle$ type Burgers vector; a_0 is the lattice parameter of a bcc cell of which the large Ni_2AlTi unit cell is composed. The creep strength of this alloy is ~3 times that of NiAl in its most creep resistant form, namely [100] axis single crystals.

NICKEL aluminide (β-NiAl) which has the CsCl, or $B2$ type structure is an important coating material in high temperature technology. The excellent oxidation and corrosion resistance properties of this alloy, however, are offset by a markedly poor resistance to high temperature creep. A specific method of strengthening NiAl which has been proposed[1,2] is the addition of an element giving rise to the extremely stable Heusler type structure. The particular Heusler structure alloy which is studied in this investigation is Ni_2AlTi. The ordering of Al and Ti atoms on one of the sublattices of the original $B2$ structure will be shown to modify the basic glide modes in such a way as to improve the high temperature creep characteristics.

The present paper is devoted to the basic aspects of high temperature creep deformation in polycrystalline Ni_2AlTi. The types of dislocations involved in glide processes in this material are first predicted on the basis of the hard sphere model, and then analyzed experimentally using transmission electron microscopy. In order to avoid possible ambiguity in determining the nature of dislocations enlarged electron micrograph images are compared with computer simulated images.

GLIDE MODE MODEL

A diagram of the Ni_2AlTi unit cell is shown in Fig. 1. It is composed of eight $B2$ or CsCl unit cells in which Ni atoms form one sublattice, and Al and Ti atoms form an ordered array on the other sublattice. The small cells constituting the large Ni_2AlTi unit cell are 1.7 pct larger in size than the NiAl unit cell.[3] This difference is sufficiently small that the magnitude of slip vectors in both NiAl and Ni_2AlTi may be expressed in terms of a_0 the lattice parameter of NiAl.

The various possible glide modes in compounds with the $B2$ type structure have been predicted on the basis of the hard sphere model by Lautenschlager, Hughes, and Brittain.[4] On the basis of these considerations the predominant slip vector in NiAl is $a_0\langle 100\rangle$. Transmission electron microscopy confirms this predominance

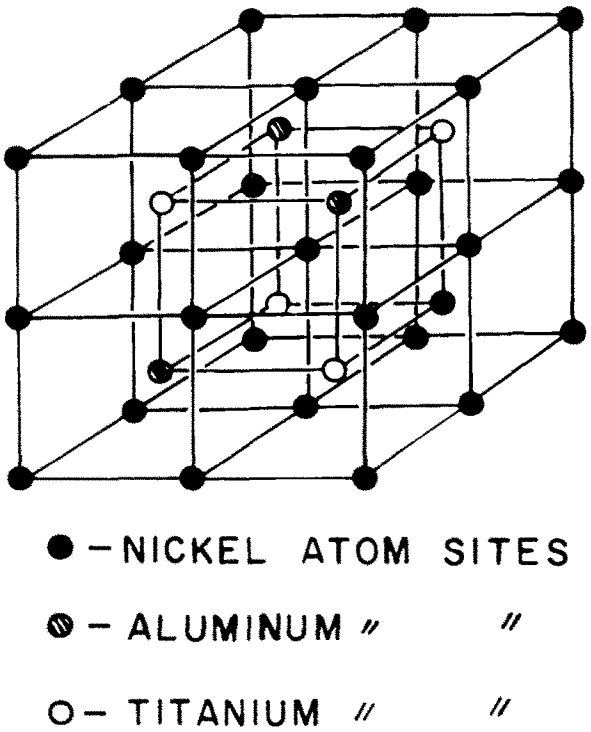

Fig. 1—Unit cell of the Heusler type structure.

of $a_0\langle 100\rangle$ type dislocations in material deformed at temperatures above 300 K.[2,5]

We now examine various possible glide modes in the A_2BC or Heusler type structure. As is the case with the $B2$ type structure the closest packed planes are of the $\{110\}$ type, and the arrangement of A, B and C atoms within a $(\bar{1}01)$ plane is shown in Fig. 2. An instructive way to consider the Heusler phase is to note that it is formed from sets of these planes arranged with a two layer repeat sequence. Possible slip translations between two adjacent $(\bar{1}01)$ planes are indicated by the vectors in Fig. 2. For this discussion, however, only one atom (C') in the second atomic layer need be considered, this is of the C atomic specie. In an $a_0[010]$ slip translation atom C' is displaced along the [010] vector shown in Fig. 2 into a position in which C atoms are now nearest neighbors. If the entire second atomic layer is considered the $a_0[010]$

P. R. STRUTT and R. S. POLVANI are Associate Professor and Research Associate, respectively, Department of Metallurgy, University of Connecticut, Storrs, Connecticut 06268. J. C. INGRAM is with the Harry Diamond Laboratories, Washington, D. C. 20438.

Manuscript submitted August 8, 1974.

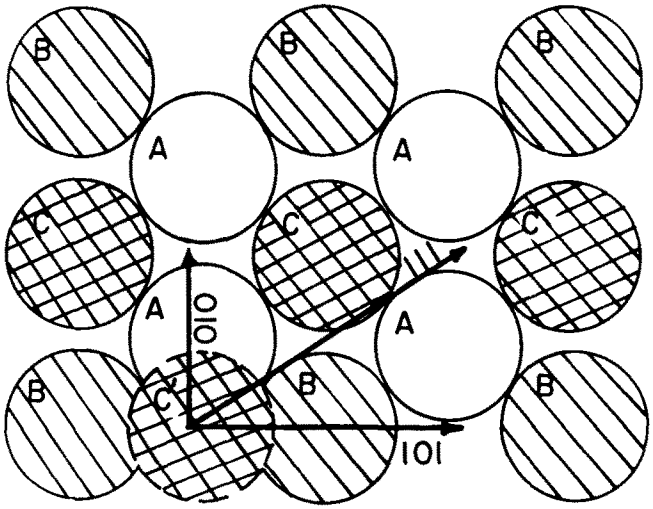

Fig. 2—Possible slip movements in the $(\bar{1}01)$ plane of the A_2BC Heusler type structure. C' is a C-type atom in an adjacent $(\bar{1}01)$ atomic layer.

translation is seen to create both B-B and C-C type wrong bonds; the fault thus formed is termed a sublattice antiphase boundary. Thus unit slip in $\langle 100 \rangle$ type directions must be accomplished by the movement of pairs of $a_0\langle 100 \rangle$ unit dislocations, in which the $a_0\langle 100 \rangle$ dislocations are coupled by a sublattice A.P.B. It is also evident that slip in $\langle 111 \rangle$ type directions is accomplished by the glide of pairs of coupled $a_0\langle 111 \rangle$ dislocations. In this case, however, a further dissociation is possible, since each of the unit $a_0\langle 111 \rangle$ dislocations may dissociate into a pair of $a_0/2\,\langle 111 \rangle$ dislocations. This dissociation of an $a_0\langle 111 \rangle$ dislocation into a pair of $a_0/2\,\langle 111 \rangle$ dislocations occurs in $B2$ structure alloys in which $\langle 111 \rangle$ slip is favored.[4] In contradistinction to $\langle 100 \rangle$, and $\langle 111 \rangle$ slip, it is clearly evident from Fig. 2 that a unit $a_0\langle 110 \rangle$ glide translation does not involve the creation of a fault. Therefore $a_0\langle 110 \rangle$ slip is accomplished by the glide of individual $a_0\langle 110 \rangle$ dislocations.

EXPERIMENTAL

Compression creep test specimens with dimensions 3.2 mm × 3.2 mm × 9.5 mm were prepared from as cast arc melted buttons of stoichiometric Ni_2AlTi. The center portion of the buttons contained long columnar grains (~1 mm in diameter) whose growth direction was along $\langle 100 \rangle$. The specimens were sectioned from this portion of the button with the compression axis along the $\langle 100 \rangle$ fiber axis. All the specimens were then annealed for 48 hours (*in vacuo* at 1473 K; the melting point temperature of Ni_2AlTi is ~1723 K. Creep tests were carried out under vacuum using a special molybdenum alloy (Climax TZM) straining jig. Axial alignment was such that kinking was non-detectable for strains up to 0.1. Barrelling was prevented by the use of a glass lubricant between the specimen end faces and the compression platens of the straining jig. The strain was measured using an LVDT extensometer.

Subsequent to mechanical creep testing transmission electron microscope samples were prepared from the compression specimens. These samples were ~0.5 mm thick and they were cut perpendicular to the compression axis. After dimpling the discs with a jet-cutter they were electropolished in a 10 pct perchloric acid methanol solution at 253 K at a potential of 10 volts. The foils were examined in a Philips 300 microscope using a ±60 deg tilt and 360 deg rotation goniometer stage. A special computer program[6] was used to facilitate the rapid orientation of the foil in obtaining a large number of two-beam conditions. As well as characterizing dislocations by the degree of visibility obtainable with different contrast conditions actual images were compared with computer simulated images. The computer method is similar to that of Head[7] but uses a different numerical procedure which reduces the computation time. The method takes into account the effect of elastic anisotropy and the values of the elastic coefficients are those for NiAl.[8]

RESULTS

Creep Behavior

The sets of creep curves shown in Fig. 3 are for tests carried out at four stress levels at 1273 K. In all cases a period of normal primary creep is followed by steady state creep. For the first 900 seconds of a test the strain increased linearly with time and $\dot{\epsilon}_i$ the instantaneous strain was taken as the slope of this line. The ratio $\dot{\epsilon}_i/\dot{\epsilon}_s$, of initial to steady state creep rate, decreases with increasing stress; this ratio is 46, 29, 25, and 7 respectively for stresses of 17.2, 34.5, 51.7 and 69.0 MN/m^2. Values of the secondary creep rates for all the tests which were performed are given in Table I.

The activation energy for steady state creep was determined from a set of creep tests in which each specimen was crept at the same stress (69 MN/m^2) but at different temperatures. In the Arrhenius plot in Fig. 4 the value of ΔH for creep is 280 kJ/mol. This value is in good agreement with that of 291 kJ/mol for self diffusion in nickel,[9] and that of 307 kJ/mol for diffusion of ^{63}Ni in stoichiometric NiAl.[10]

The stress dependence of the creep rate is shown in Fig. 5, where normalized steady state creep rate $\dot{\epsilon}\exp \Delta H/KT$ is plotted as a function of tensile stress. For comparative purposes data for NiAl [001] axis crystals[11] is included in Fig. 5, and it is well evident that the polycrystalline Ni^2AlTi has a significantly

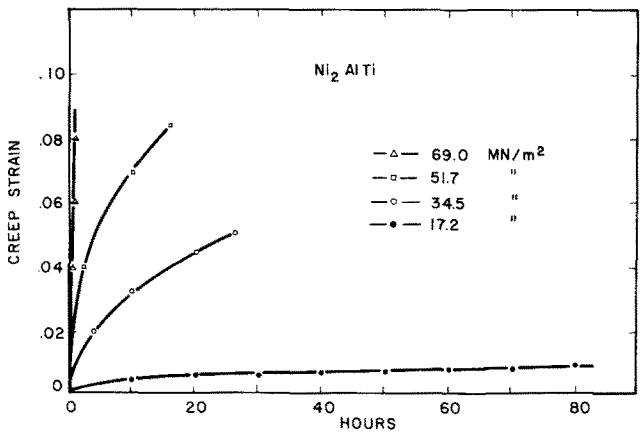

Fig. 3—Creep curves for stoichiometric Ni_2AlTi at 1273 K.

Table I. Summary of Polycrystalline Ni_2AlTi Creep Data, $\dot{\epsilon}_s$ is the Steady State Creep Rate

Specimen No.	Applied Stress MN/m²	Applied Stress k.s.i.	Temperature K	Temperature °C	T/T_m	$\dot{\epsilon}_s$ (s^{-1})
4	17.2	2.5	1273	1000	0.74	2.82×10^{-8}
1	34.5	5	1273	1000	0.74	2.52×10^{-7}
3	51.7	7.5	1273	1000	0.74	6.19×10^{-7}
13	69.0	10	1026	753	0.60	2.36×10^{-8}
17	69.0	10	1048	775	0.61	4.21×10^{-8}
12	69.0	10	1058	785	0.61	5.72×10^{-8}
16	69.0	10	1088	815	0.63	1.33×10^{-7}
15	69.0	10	1124	851	0.65	3.42×10^{-7}
18	69.0	10	1173	900	0.68	7.72×10^{-7}
2	69.0	10	1273	1000	0.74	7.65×10^{-6}
8	82.7	12	1073	800	0.62	2.83×10^{-7}
7	103.4	15	1023	750	0.59	1.83×10^{-7}
5	103.4	15	1148	875	0.67	6.50×10^{-6}

higher creep strength than nickel aluminide in its most creep resistant form.[11] Specifically, compared with a NiAl [001] axis crystal, three times the stress must be applied to Ni_2AlTi to maintain a normalized creep rate ($\dot{\epsilon}$ exp $\Delta H/kT$) of 10^7 s^{-1}.

Finally, for Ni_2AlTi, the stress exponent n in the creep equation $\dot{\epsilon} = \sigma^n \exp -\Delta H/kT$ varies from a value of 3 at low stresses to a value of 13 at high stresses.

Dislocation Analysis

Several electron microscope diffraction contrast experiments were carried out in order to (i) determine the Burgers vector of isolated dislocations, (ii) analyze dislocation reactions within nodal networks, and (iii) analyze dislocation networks within simple sub-boundaries.

Electron micrographs forming part of a contrast analysis experiment on a thin foil region containing three isolated sloping dislocations *A*, *B*, and *C* are shown in Fig. 6. The foil, whose normal was close to [001], was sectioned from a specimen crept at 69 MN/m_2 at 1123 K. In the complete analysis two ⟨200⟩, six ⟨110⟩ and ten ⟨112⟩ reflections were used. The axis of dislocations *A*, *B*, *C* are closely parallel to the [011], [$\bar{1}$01] and [111] directions respectively. These were determined by first finding the projected direction of each dislocation for several foil orientations. The actual direction of a dislocation is then given by the intersection point on the stereographic projection of a set of great circles, each representing the plane containing the beam direction and the projected dislocation axis.

In proceeding to analyze dislocations *A*, *B* and *C* it should be noted that for each two beam condition all three dislocations tend to have a similar appearance; an obvious indication that they probably have the same Burgers vector. Next, in Figs. 6(*b*), (*c*), and (*d*) dislocation *A* appears to be invisible for $\bar{g} = [\bar{2}00]$, $[0\bar{1}1]$, and $[\bar{2}\bar{1}1]$, and a tentative application of the $\bar{g} \cdot \bar{b} = 0$ invisibility condition shows $\bar{b} = a_0[011]$. Since *A* lies very close to [011] it appears to be a screw dislocation lying along an evenfold symmetry axis. In this case the $\bar{g} \cdot \bar{b} = 0$ condition is fully valid, since even in an anisotropic crystal the only elastic displacement

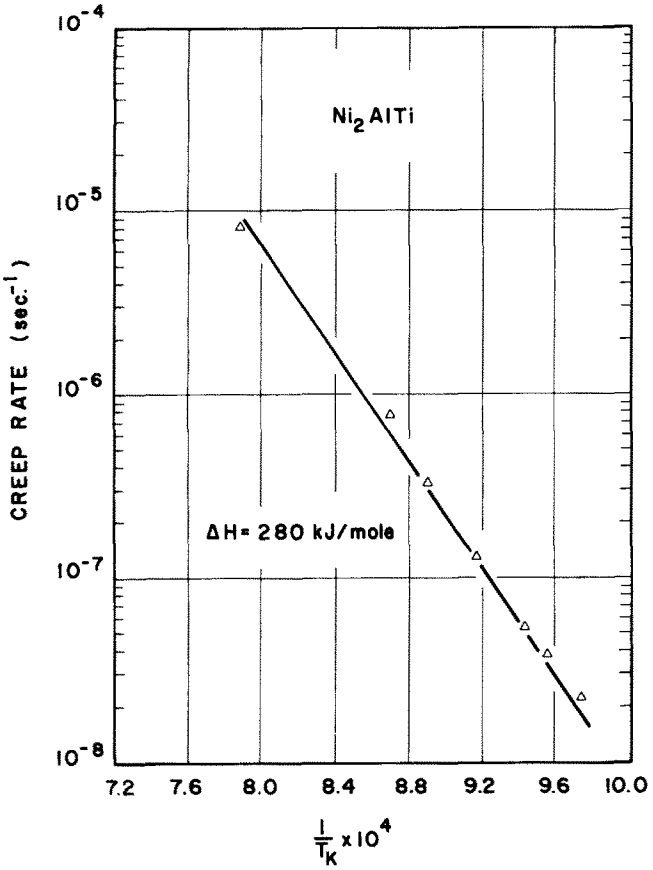

Fig. 4—An Arrhenius plot of $ln\ \dot{\epsilon}_S$ *vs* $1/T_K$ for stoichiometric Ni_2AlTi for a stress of 69 MN/m^2. The value of ΔH is 280 kJ/mol.

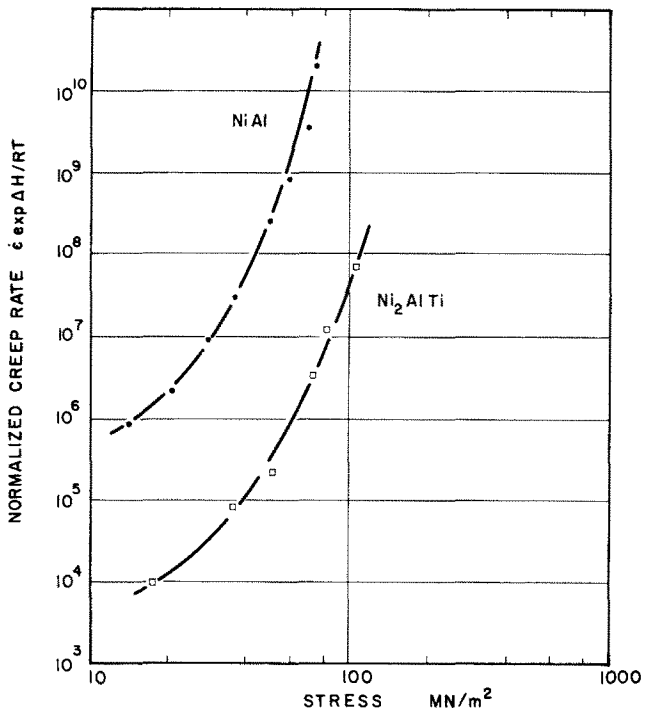

Fig. 5—Normalized creep rate $\dot{\epsilon}$ exp $\Delta H/kT$ plotted as a function of stress. The curve for [001] axis NiAl single crystals is included as a basis of comparison.

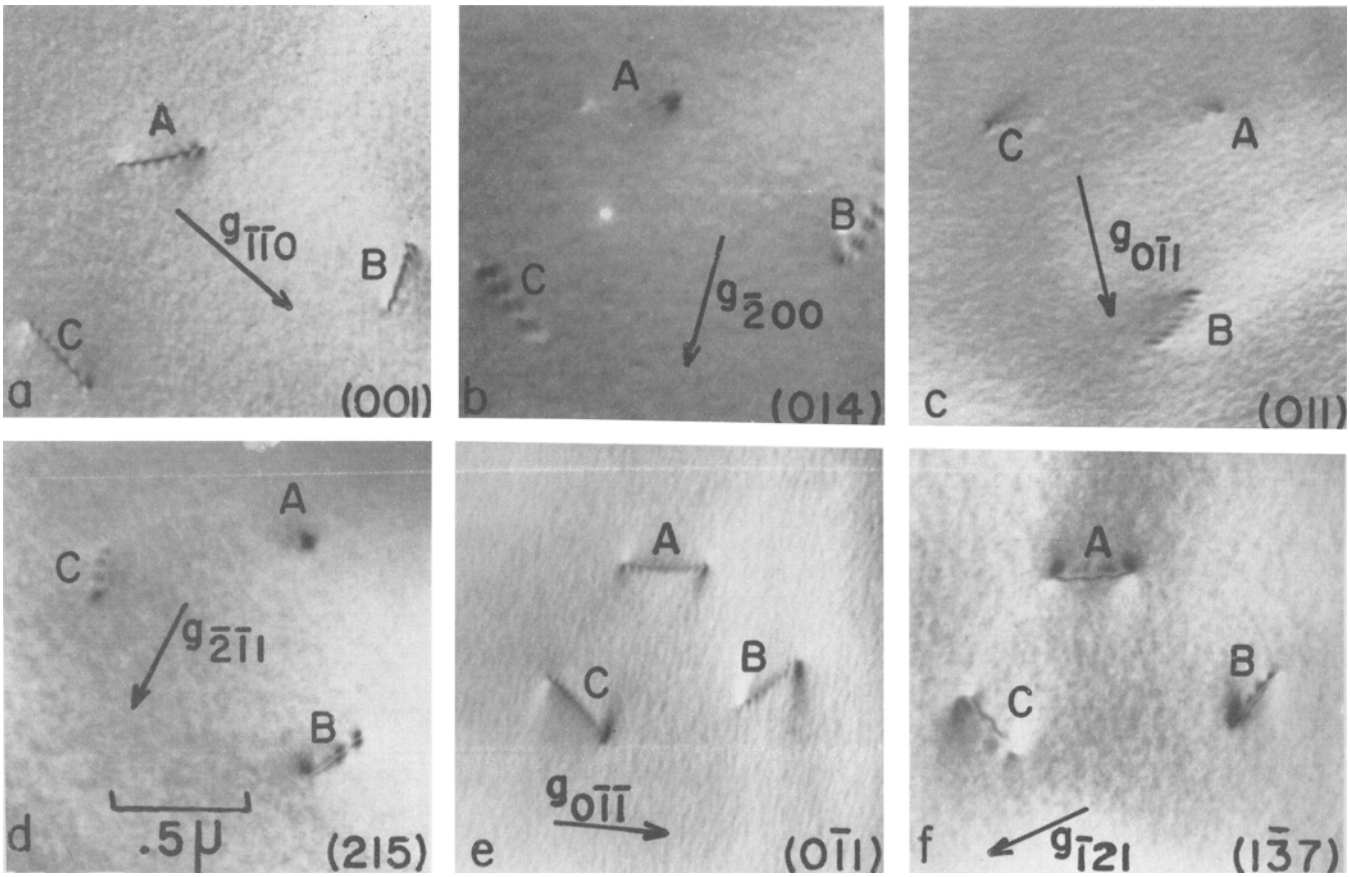

Fig. 6—Part of a Burgers vector analysis of three isolated sloping dislocations in a Ni_2AlTi specimen deformed in creep. The three dislocations are deduced to have an $a_0\langle 001\rangle$ Burgers vector. The plane perpendicular to the beam direction is indicated in the lower right hand corner of the micrographs.

is along the dislocation axis; thus the residual contrast at the intersection with one surface (and both surfaces in Fig. 6(*b*)) is presumably due to surface relaxation.[12] The analyses for dislocations *B* and *C* are more complex, since conditions of apparent invisibility (or near invisibility) are not attainable. However, it becomes clearly evident that these dislocations, like dislocation *A*, have an $a_0[011]$ Burgers vector when enlarged contrast images are compared with computer simulated images. In Figs. 7(*a*) and (*b*) there is excellent agreement between the actual and simulated images for dislocations *B* and *C* respectively for the conditions $\bar{g}\cdot\bar{b} = 0$, and $\bar{g}\cdot\bar{b} = -2$ respectively.

For dislocations *B* and *C* strong residual contrast in Figs. 6(*b*), (*c*) and (*d*) arises from non-zero values of $\bar{g}\cdot\bar{b}\times\bar{u}$, and $\bar{g}\cdot\bar{b}_e$, where $\bar{b}_e$ is the edge component of $\bar{b}$.[13] In addition, an effect arises from displacements in the dislocation strain field due to the elastic anisotropy of the crystal. There is a striking case of strong residual contrast in Fig. 6(*b*) for dislocation *C* where there is a strong double image when both $\bar{g}\cdot\bar{b}$ and $\bar{g}\cdot\bar{b}\times\bar{u}$ are both zero. This degree of contrast arises from a non-zero value of $\bar{g}\cdot\bar{b}_e$ (equal to 4/3) and anisotropic elastic displacements.

Finally, concerning the contrast analysis of dislocation *C*, there is again excellent agreement between the actual, and simulated images in Fig. 7(*c*); in this case $\bar{g}\cdot\bar{b} = 3$. Thus it is conclusive that the three dislocations in Fig. 6 have the same Burgers vector, namely $\bar{b} = a_0[011]$.

In the present study only $a_0\langle 110\rangle$ type dislocations have been observed in the single phase Ni_2AlTi alloy. However, pairs of $a_0\langle 100\rangle$ dislocations coupled with a sublattice A.P.B. are observed in Ni_2AlTi when this is a coexistent phase in a two phase Ni-Al-Ti alloy.[14]

Examples of reactions between $a_0\langle 110\rangle$ dislocations in Ni_2AlTi formed in creep are shown in Fig. 8; Table II lists the Burgers vectors and axes of the dislocations. In discussing part of the analysis of eight dislocations in Fig. 8, major attention is devoted to the three dislocations (1, 2 and 3) which form one of the nodes. Dislocation 1 appears to be essentially invisible in Figs. 8, (*b*) and (*f*), therefore $\bar{b}$ is deduced to be $a_0[101]$. This infers that in Figs. 8(*a*) and (*g*) $\bar{g}\cdot\bar{b}$ is -2 for dislocation 1. This is a contrast condition giving rise to a double image, and careful examination of the micrographs reveals doublet contrast images. As shown by computer simulated images for $\bar{g}\cdot\bar{b} = \pm 2$ the intensity of the individual peaks of a doublet may vary appreciably. For example in Fig. 8(*a*) dislocation 2 does not appear to have a double image for $\bar{g}\cdot\bar{b} = +2$. In an enlargement of this image in Fig. 9(*a*) an extremely faint subsidiary peak is just discernible to the left of the main peak. It is also evident in the corresponding computer picture in Fig. 9(*a*), which is actually for a higher lateral magnification. The characterization of dislocation 2 as having a Burgers vector of $a_0[\bar{1}10]$ is based on (i) invisibility for $\bar{g}\cdot\bar{b} = 0$ in Fig. 8(*h*), and (ii) contrast corresponding to $\bar{g}\cdot\bar{b} = +2$ in Figs. 8(*a*), (*b*), and (*e*). Since dislocations 1 and 2 are

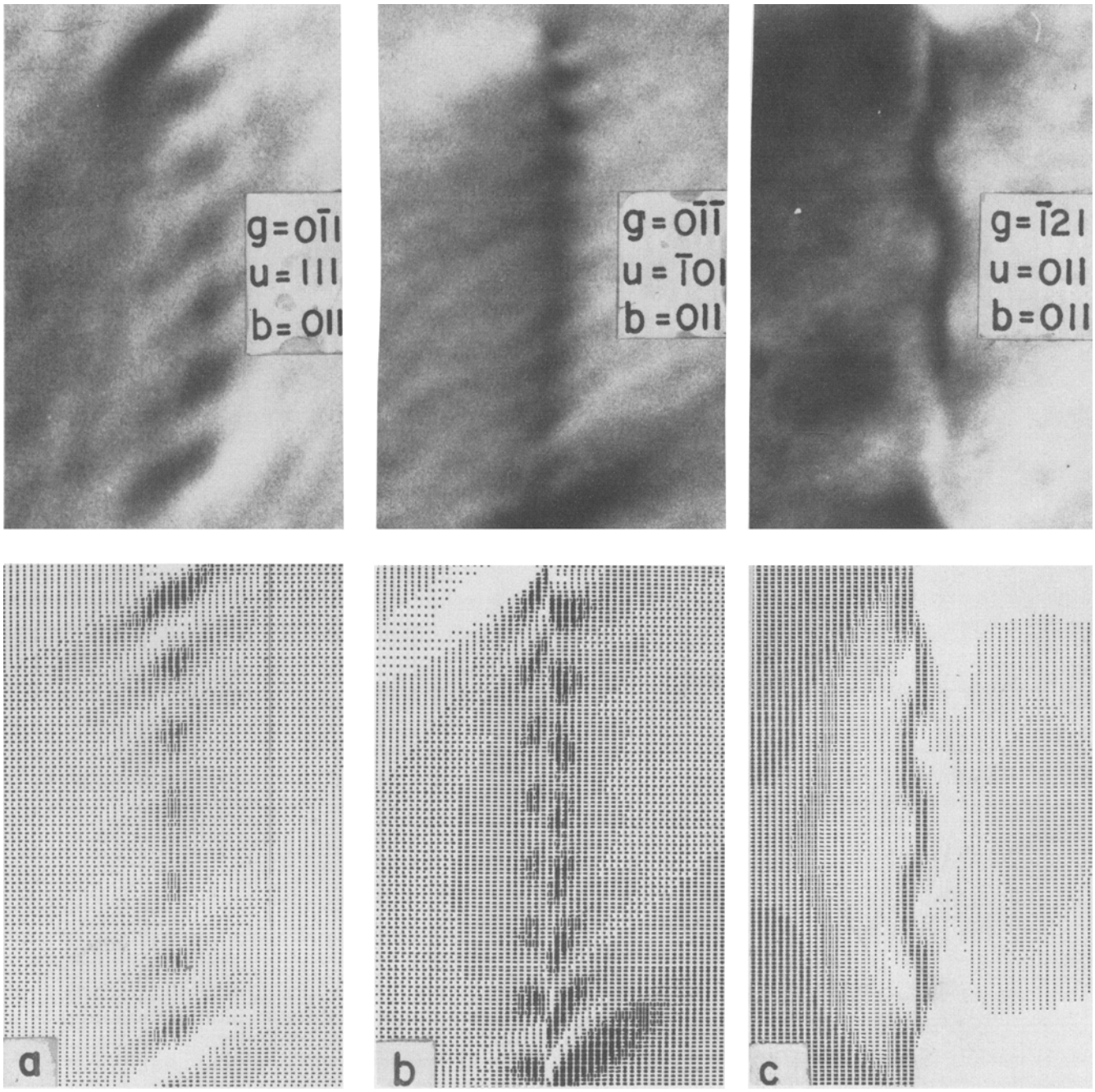

Fig. 7—A comparison between the actual and computer simulated images for (i) dislocation B in Fig. 6(c), (ii) dislocation C in Fig. 6(e), and (iii) dislocation C in Fig. 6(f).

deduced to have Burgers vectors of $a_0[101]$ and $a_0[\bar{1}10]$ that of dislocation 3 has to be $a_0[0\bar{1}\bar{1}]$ to maintain Burger vector conservation at the node. This deduction was verified by contrast analysis since invisibility with $\bar{g}\cdot\bar{b} = 0$ is evident with $\bar{g} = [\bar{2}00]$ and $[01\bar{1}]$ in Figs. 8(a) and (d) respectively. Well defined images for $\bar{g}\cdot\bar{b} = -1$ are seen in Figs. 8(e), (f) and (h) for $\bar{g} = [\bar{1}10]$, $[\bar{1}01]$ and $[110]$, similarly in Figs. 8(g) for $\bar{g} = [\bar{1}0\bar{1}]$. Double images for $\bar{g}\cdot\bar{b} = 2$ and -2 respectively are seen in Figs. 8(c) and (b) for $\mathbf{g} = [011]$ and $[020]$.

Another node where a similar type reaction occurs is formed by the junction of dislocations 5, 6 and 7, which have Burgers vectors of $[011]$, $[\bar{1}\bar{1}0]$ and $[10\bar{1}]$ respectively. An unusual feature in the analysis of these dislocations is the strong double image of dislocation 7 in Fig. 8(b) for $\bar{g}\cdot\bar{b} = 0$. In Fig. 9(b) a computer simulated image of this dislocation (which lies nearly parallel to the foil surfaces) displays a wide intense double image even though $\bar{g}\cdot\bar{b} = 0$. It should be pointed out however that $\bar{g}\cdot\bar{b}_e$ and $\bar{g}\cdot\bar{b}\times\bar{u}$ are appreciable in this case, namely $-4/5$, and $8/\sqrt{30}$ and these quantities are responsible for the strong image. In contradistinction it is seen that dislocations 4 and 8, although having the same $\bar{b}$ as dislocation 7 are near the screw orientation, thus the quantities $\bar{g}\cdot\bar{b}_e$ and $\bar{g}\cdot\bar{b}\times\bar{u}$ are exceedingly small. These dislocations are

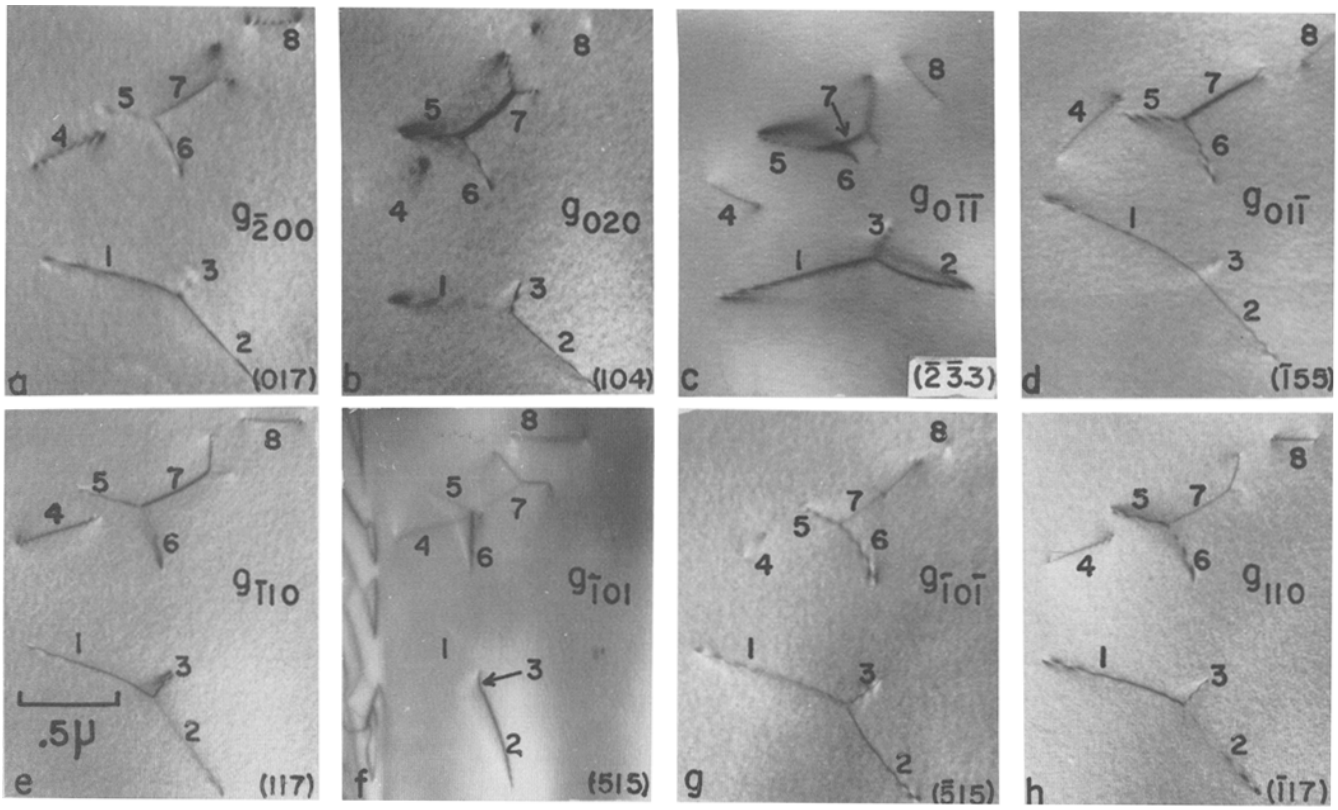

Fig. 8—Part of a Burgers vector analysis of a nodal dislocation network formed during creep. All dislocation segments are deduced to have an $a_0\langle 110\rangle$ type Burgers vector. Plane perpendicular to the beam direction is shown in the lower right hand corner of the micrographs.

Table II. The Burgers Vector $\bar{b}$, and Dislocation Axis $\bar{u}$ for Each Dislocation in Fig. 8

Dislocation	$\bar{b}$	$\bar{u}$
1	101	$5\bar{2}3$
2	$\bar{1}10$	$2\bar{3}1$
3	$0\bar{1}\bar{1}$	443
4	$\bar{1}01$	$\bar{1}01$
5	011	$\bar{5}21$
6	$\bar{1}\bar{1}0$	$1\bar{3}2$
7	$10\bar{1}$	$\bar{5}\bar{2}1$
8	$10\bar{1}$	$\bar{5}15$

Table III. Values of $\bar{g}\cdot\bar{b}$ for Three $a_0\langle 110\rangle$ Type Dislocations Forming the Network in Fig. 10

	$\bar{g}$					
$\bar{g}\cdot\bar{b}$	$0\bar{2}0$ (*a*)	200 (*b*)	$\bar{1}10$ (*c*)	$\bar{1}\bar{1}0$ (*d*)	$\bar{1}01$ (*e*)	$01\bar{1}$ (*f*)
$\bar{g}\cdot\bar{b}_1$	−2	+2	0	−2	−1	+1
$\bar{g}\cdot\bar{b}_2$	+2	0	−1	+1	−1	0
$\bar{g}\cdot\bar{b}_3$	0	−2	+1	+1	+2	−1

then essentially invisible in Fig. 8(*b*) for $\bar{g} = [020]$, and the residual contrast is due to elastic displacements arising from surface relaxation.[12] Examination of the micrographs in Fig. 8 reveals the contrast patterns along dislocations 4 and 8 are reversed with respect to each other, thus they are similar type dislocations with opposite sign Burgers vectors. Finally, Fig. 9(*c*) shows a computer simulated image for dislocation 5 in Fig. 8(*d*), for $\mathbf{g} = [01\bar{1}]$.

In summary, all the eight dislocation segments in Fig. 8 have been shown to have an $a_0\langle 110\rangle$ type Burgers vector, as did in fact the three isolated dislocations in Fig. 6.

This section on the characterization of dislocations, and dislocation networks in Ni_2AlTi concludes with an analysis of a simple sub-boundary. An inherent difficulty in an analysis of this type is that even with a fairly open network the dislocation segments are too short for the use of computer simulated pictures. A consistent analysis of dislocations in the network in Fig. 10 is based on the following criteria.

(i) Each dislocation segment has an $a_0\langle 110\rangle$ type Burgers vector. This is in view of the previous analyses, and the fact that $a_0\langle 100\rangle$ dislocations occur in pairs coupled by a sublattice A.P.B.[14]

(ii) The vectorial sum of the Burgers vectors of dislocations intersecting at a node is zero.

(iii) For $\bar{g}\cdot\bar{b} = 0$ dislocations are generally invisible or in faint contrast. For $\bar{g}\cdot\bar{b} = +2$, or -2 dislocations display a double image with either, both peaks in weak contrast, or one well delineated whilst the other is very faint.

For the purpose of identification the sides of the numbered inserts in Figs. 10(*a*), and (*d*) are aligned parallel to the segments of the hexagonal type dislocation network. First, considering dislocation segments parallel to direction 1, these are completely invisible in Fig. 10(*c*) for $\bar{g} = [\bar{1}10]$, hence assuming (i) above, the Burgers vector $\bar{b}$, is $a_0[110]$. The faint contrast in Figs. 10(*b*), and (*d*) then corresponds to $\bar{g}\cdot\bar{b}_1 = +2$, and

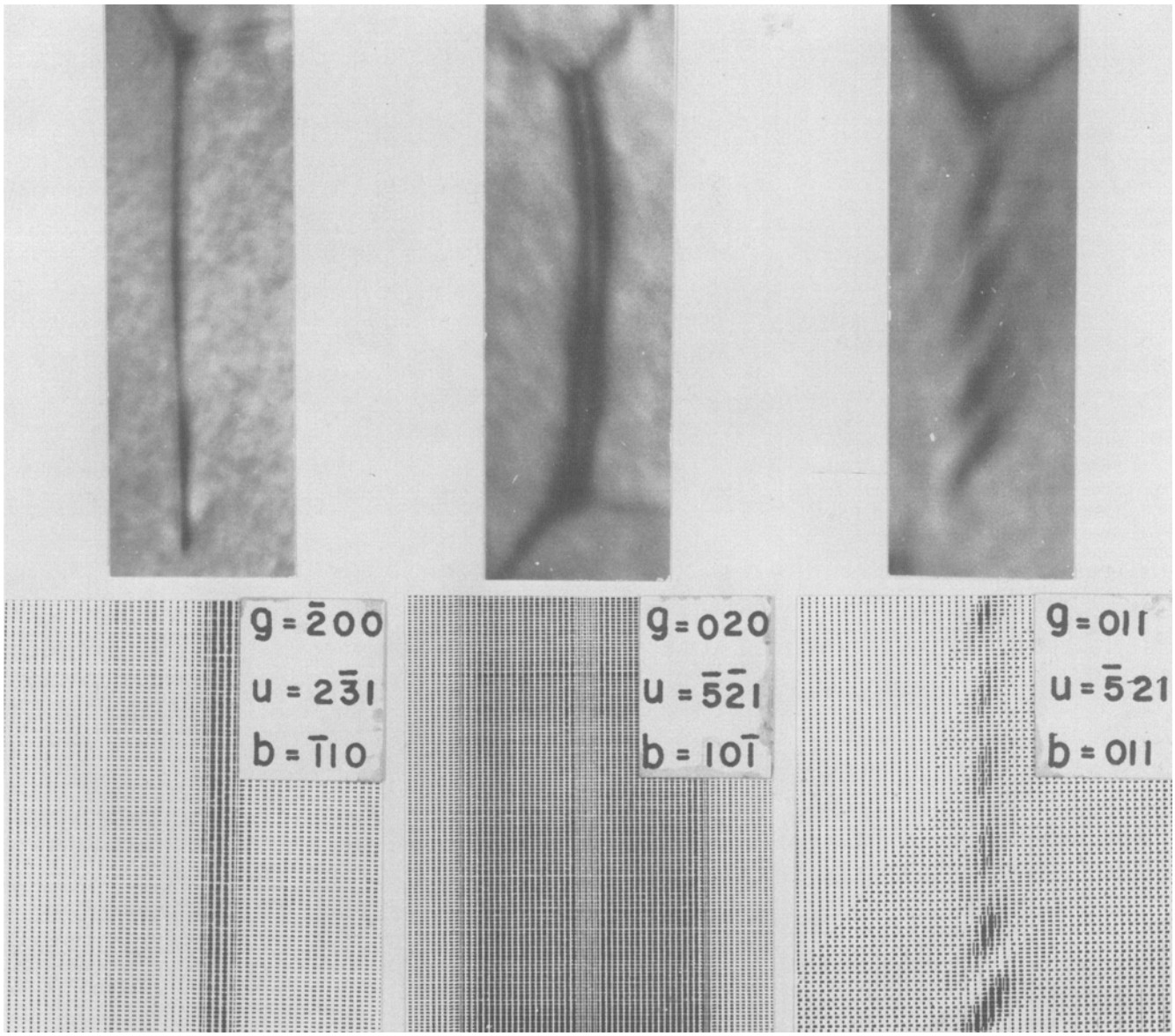

(a) (b) (c)

Fig. 9—A comparison between actual and simulated images of dislocations 2, 7, and 5 in Fig. 8(*a*), (*b*), and (*d*) respectively.

-2 respectively. The contrast in Fig. 10(*a*) for $\bar{g} = [0\bar{2}0]$ where $\bar{g} \cdot \bar{b}_1 = -2$ shows a double image with a strong and weak peak. Strong single image contrast is evident in Figs. 10(*e*) and (*f*) for $\bar{g} = [\bar{1}01]$ and $[01\bar{1}]$. and this corresponds to $\bar{g} \cdot \bar{b}_1$ equal to -1 and $+1$ respectively.

By employing similar reasoning, and applying criteria (i) through (iii), it may be shown that dislocation segments 2 and 3 have Burgers vectors of $a_0[0\bar{1}\bar{1}]$ and $a_0[\bar{1}01]$ respectively. The values of $\bar{g} \cdot \bar{b}$ for dislocation segments 1, 2, and 3 for each operative reflection are summaried in Table III.

DISCUSSION

A significant feature of this investigation is that only $a_0\langle 110\rangle$ dislocations were observed in single phase Ni_2AlTi. This is in contrast to the predominance of $a_0\langle 100\rangle$ dislocations in NiAl.[2,5] Unlike NiAl however, considerations based on the hard sphere model (see Fig. 2) show that $\langle 100\rangle$ glide involves the glide of pairs of $a_0\langle 100\rangle$ dislocations coupled by a sublattice A.P.B. In NiAl $\langle 110\rangle$ glide although predicted[4] is not observed,[2,5] thus it is concluded that $a_0\langle 100\rangle$ dislocations have a higher mobility than $a_0\langle 110\rangle$ dislocations. However, in the Heusler structure $\langle 110\rangle$ slip is favored since $\langle 100\rangle$ slip involves the formation of a sublattice antiphase boundary.

The foregoing considerations relate solely to the nature of the operative slip systems. In comparing the creep behavior of NiAl and Ni_2AlTi it is also necessary to consider the dislocation climb velocity v, and the mean dislocation slip length L. The creep rate $\dot{\epsilon}$ depends on these quantities via Eq. [1], this form of

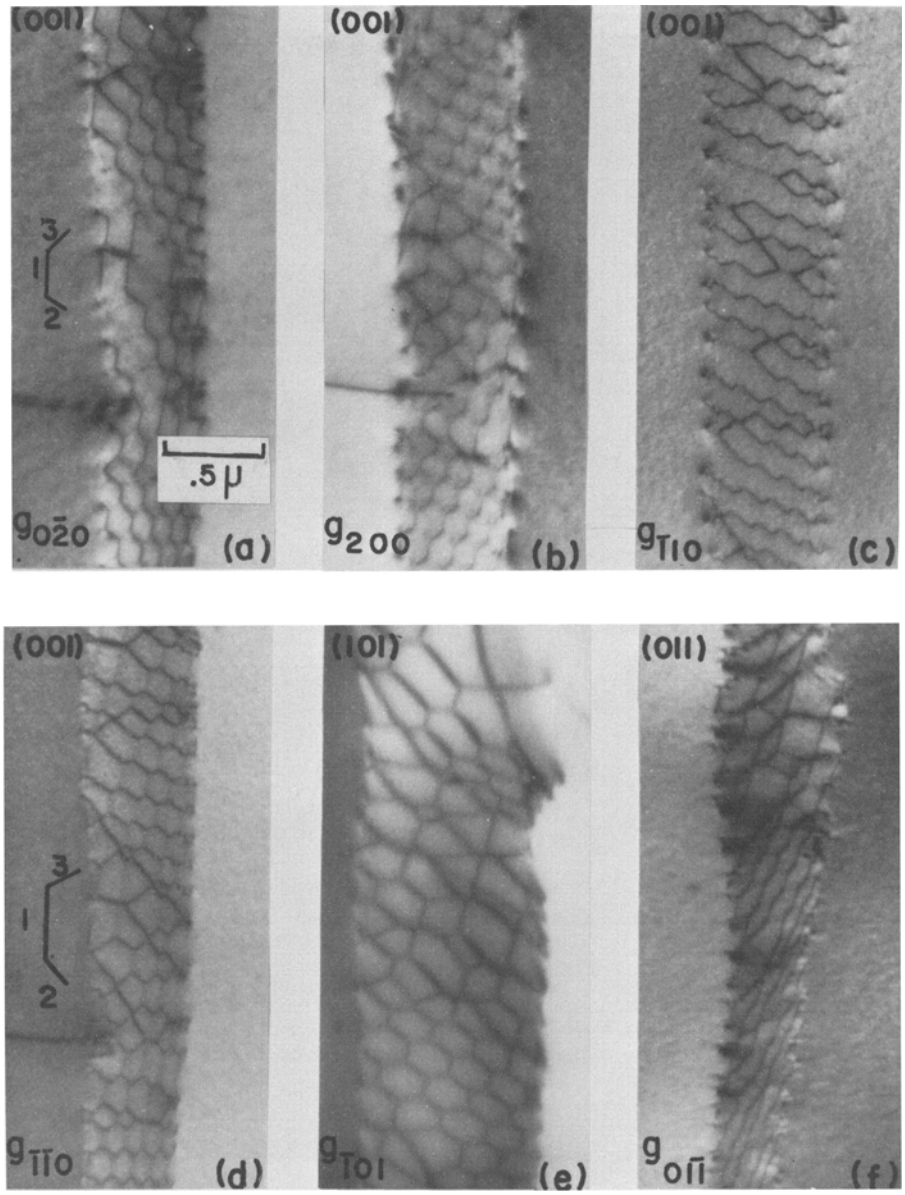

Fig. 10—A hexagonal-type network formed during creep in Ni_2AlTi, the network results from the reaction of $a_0\langle 110\rangle$ type dislocations. Plane perpendicular to the beam direction is shown in the upper left hand corner of the micrographs.

the Taylor relation is used in various creep models.[16]

$$\dot{\epsilon} = N\mathbf{b}\omega(v)A(L) \qquad [1]$$

Here N is the number of dislocation sources per cm^{-3}, $\mathbf{b}$ the Burgers vector, and $\omega(v)$ the frequency with which arrested dislocations successfully overcome obstacles. The area $A(\sim L^2)$ is that swept out by a dislocation after having overcome an obstacle. If diffusion is the rate controlling process then ω is proportional to the climb velocity v, which is given by Eq. [2].[17]

$$V = \frac{Dv_a(F/L)}{\mathbf{b}_e^2 kT} \qquad [2]$$

In this expression D is the diffusion coefficient, v_a the atomic volume, F/L the force per cm acting on the dislocation, and $\mathbf{b}_e$ the Burgers vector of the dislocation edge component; k and T have the usual meaning. In this discussion we wish to compare the relative climb mobility of $a_0\langle 100\rangle$ dislocations in NiAl with that of $a_0\langle 110\rangle$ dislocations in Ni_2AlTi. Although a direct comparison is not possible an approximate idea is obtained by comparing climb mobilities of $a_0\langle 100\rangle$ and $a_0\langle 110\rangle$ dislocations in the same crystal structure. From Eq. [2] the climb velocities of these two types of dislocations (for the same value of F/L) differ by a factor of two. In view of this it appears that $a_0\langle 100\rangle$ dislocations in NiAl and $a_0\langle 110\rangle$ dislocations in Ni_2AlTi climb with about equal facility.

It is proposed that the higher creep strength of Ni_2AlTi, whilst not attributable to a decreased dislocation climb mobility is due in part to an inability for $a_0\langle 110\rangle$ dislocations to undergo cross-slip in the Heusler structure. Firstly, an $a_0\langle 110\rangle$ screw dislocation cannot transfer from one $\{110\}$ plane to another, as planes of this type do not intersect in a $\langle 110\rangle$ direction. Secondly, the hard sphere model suggests that shear on a cube plane directly along a $\langle 110\rangle$ direction is highly improbable.[4] The only alternative way for accomplishing $\langle 110\rangle\{001\}$ shear is by the dissociation given by Eq. [3]; the fault is a sublattice A.P.B.

$$a_0[110] \rightarrow a_0[100] + \text{fault} + a_0[010] \qquad [3]$$

Again, this type of shear, which involves the motion

of a dislocation/fault pair will be difficult in comparison to simple $\langle 110 \rangle \{110\}$ shear. From the preceding considerations it is concluded that the cross-slip of $a_0\langle 110 \rangle$ dislocations in Ni_2AlTi is unlikely to occur. This eliminates one way by which dislocations may circumvent obstacles during creep.

Quantitatively this results in a value of A in Eq. [1] which may be significantly smaller than that for NiAl. The area A is $\sim L^2$, where L is the average dislocation slip distance.

Finally, another source of creep strengthening in Ni_2AlTi may be the highly stabilized dislocation networks formed by the reaction of $a_0\langle 110 \rangle$ dislocations. Obviously the reaction of two $a_0\langle 110 \rangle$ dislocations is strongly favorable energetically. In NiAl the reaction of $a_0\langle 100 \rangle$ dislocations may reduce the anisotropic elastic strain energy,[2,18,19] but not by a comparable amount. The reaction of $a_0\langle 110 \rangle$ dislocations in Ni_2AlTi is clearly analogous to that between $a_0/2\langle 110 \rangle$ dislocations in fcc metals, where hexagonal networks form with great facility during high temperature deformation.[20]

ACKNOWLEDGMENT

The work described in this paper was supported by the National Science Foundation under Grant DMR75-05231.

REFERENCES

1. P. R. Strutt and G. M. Rowe: *29th Annual Meeting, Electron Microscope Society of America,* 1971, vol. 29, p. 116.
2. P. R. Strutt, G. M. Rowe, J. C. Ingram, and Y. H. Choo: *Electron Microscopy and Structure of Materials,* p. 722, University of California Press, Berkeley, California, 1972.
3. A. Taylor and R. W. Floyd: *J. Inst. Metals,* 1952-53, vol. 80, p. 25.
4. E. P. Lautenschlager, T. Hughes, and J. O. Brittain: *Acta Met.,* 1967, vol. 15, p. 1347.
5. M. H. Loretto and R. J. Wasilewski: *Phil. Mag.,* 1972, vol. 23, p. 1311.
6. Wen-Shian Tzeng and P. R. Strutt: *31st Annual Meeting, Electron Microscope Society of America,* 1973, vol. 31, p. 100.
7. A. K. Head: *Austral. J. Phys.,* 1967, vol. 20, p. 557.
8. R. J. Wasilewski: *Trans. TMS–AIME,* 1966, vol. 236, p. 455.
9. A. Y. Shingaer: *Phys. Metals Metallog.,* 1963, vol. 15, p. 100.
10. G. F. Hancock and B. R. McDonnel: *Phys. Stat. Solidi (a),* 1971, vol. 4, p. 143.
11. Y. H. Choo: M. S. Thesis, University of Connecticut, 1971.
12. W. J. Tunstall, P. B. Hirsch, and J. Steeds: *Phil. Mag.,* 1964, vol. 9, p. 99.
13. A. Howie and M. J. Whelan: *Proc. Roy. Soc.,* 1962, vol. A267, p. 206.
14. P. R. Strutt, Wen-Shian Tzeng, and R. S. Polvani: *Met. Trans. A,* 1976, vol. 7A, pp. 33-40.
15. D. I. Potter: *Mater. Sci. Eng.,* 1969-70, vol. 5, p. 201.
16. P. R. Strutt and R. A. Dodd: *Ordered Alloys, Physical Metallurgy and Structural Applications,* p. 475, Clatior's, Baton Rouge, 1970.
17. J. P. Hirth and J. Lothe: *Theory of Dislocations,* p. 513, McGraw-Hill, New York, 1968.
18. N. J. Zaluzec and H. L. Fraser: *Scr. Metal.,* 1974, vol. 8, p. 1049.
19. P. R. Strutt, R. A. Dodd, and G. M. Rowe: *Proc. 2nd Int. Conf. on the Strength of Metals and Alloys,* p. 1057, Amer. Soc. Met., 1970.
20. V. K. Lindross and H. M. Miekk-Oja: *Phil. Mag.,* 1968, vol. 17, p. 119.